

RESEARCH ARTICLE

Impedance spectroscopy: A useful technique to unveil the mechanism of a CO oxidation reaction

Emerson Luiz dos Santos Veiga¹  | Héctor Beltrán-Mir¹  | Xavier Vendrell²  |
Jordi Llorca³ | Eloísa Cordoncillo¹

¹Departamento de Química Inorgánica y Orgánica, Universitat Jaume I, Castellón de la Plana, Spain

²Departamento de Química Inorgánica y Orgánica, Universitat de Barcelona, Barcelona, Spain

³Institute of Energy Technologies, Department of Chemical Engineering and Barcelona Research Center in Multiscale Science and Engineering, Universitat Politècnica de Catalunya, Barcelona, Spain

Correspondence

Héctor Beltrán-Mir and Eloísa Cordoncillo, Departamento de Química Inorgánica y Orgánica, Universitat Jaume I, 12071 Castellón de la Plana, Spain.
Email: mir@uji.es and cordonci@uji.es

Funding information

Spanish Ministerio de Ciencia e Innovación, Grant/Award Number: PID2020-116149GB-I00; Generalitat Valenciana, Grant/Award Number: GRISOLIA/2019/054; Generalitat de Catalunya; ICREA Academia program and projects MICINN/FEDER, Grant/Award Numbers: PID2021-124572OB-C31, GC 2021 SGR 01061

Abstract

In this work, the impedance spectroscopy (IS) technique was used to aid in understanding the reaction mechanism of the CO oxidation reaction using the $\text{Pr}_2\text{Zr}_{2-x}\text{Fe}_x\text{O}_{7\pm\delta}$ ($x = 0$ and 0.10) mixed oxide as a heterogeneous catalyst. The catalytic reaction occurred in the same temperature range where there was a decrease in the overall resistivity of the materials. Moreover, it has been observed that within the temperature range where the catalytic process takes place, there is a variation in the A and n parameters of the power law dispersion. Combining IS with catalytic reactions offers a robust approach to enhance the understanding of the mechanisms involved in the CO oxidation reaction. It enables precise analysis of the changes that take place at the solid–gas interface, particularly the generation of reactive oxygen species. Furthermore, it allows examining the relationship between the presence of oxygen vacancies and defects, which directly impact the catalytic process.

KEYWORDS

CO oxidation, heterogeneous catalysis, impedance spectroscopy, Pr and Fe

1 | INTRODUCTION

Impedance spectroscopy (IS) is a widely used technique for investigating the kinetics of electrochemical reactions and the electrical properties of materials and their interfaces. As catalysis is predominantly influenced by surface

effects, the IS technique is particularly useful for studying phenomena occurring at the solid–gas interface and can provide insights into the mechanisms of catalytic reactions by analyzing changes in total resistivity under different atmospheric conditions. Thus, IS can be used to interpret catalytic mechanisms by examining the mobility of charge

This is an open access article under the terms of the [Creative Commons Attribution](https://creativecommons.org/licenses/by/4.0/) License, which permits use, distribution and reproduction in any medium, provided the original work is properly cited.

© 2023 The Authors. *Journal of the American Ceramic Society* published by Wiley Periodicals LLC on behalf of American Ceramic Society.

carriers in bulk or interfacial regions, as well as the role of oxygen vacancies in material conduction.^{1,2}

The IS requires measuring the sample over a range of frequencies from 10 Hz to 10 MHz at different temperatures in order to separate the different regions that contribute to the overall sample resistance. The resistive (R) and capacitive (C) components of the impedance can be determined by applying a voltage across the sample and measuring the current response. Each region of the sample has different relaxation times and time constants, τ , given by the product of R and C (Equation 1). It is possible to separate the regions of the sample on a frequency scale depending on the relaxation time of each region in Equation (2)³⁻⁵:

$$\tau = RC \quad (1)$$

$$\omega_{\max} RC = 1 \quad (2)$$

where ω_{\max} is the frequency of maximum loss and can be expressed by the formula $\omega_{\max} = 2\pi f_{\max}$.³

In a ceramic, most electrically distinct regions can be characterized by different parallel RC elements. Each parallel RC element corresponds to a semicircle in the complex plane plots, Z^* , and can be transformed into three other complex formalisms: admittance (Y^*), electric modulus (M^*), and permittivity (ϵ^*).^{3,6} These formalisms are interrelated by $Z^* = 1/Y^*$; $M^* = j\omega C_0 Z^*$; $\epsilon^* = 1/M^*$; $Y^* = j\omega C_0 \epsilon^*$; where C_0 is the vacuum capacitance of the conductive cell. Each has real and imaginary components, usually given by $Z^* = Z' - jZ''$; $M^* = M' + jM''$; $\epsilon^* = \epsilon' - j\epsilon''$; $Y^* = Y' + jY''$.⁷

Following these equations, the data can be represented as either complex plane plots (also called Nyquist plot), for example, Z'' versus Z' , or as spectroscopic plots of the imaginary part of the Z'' and M'' versus $\log f$.

In the representation of Z'' and M'' versus $\log f$, a Debye peak arises, which can be described by^{8,9}

$$Z'' = R \left[\frac{\omega RC}{1 + (\omega RC)^2} \right] \quad (3)$$

$$M'' = \frac{\epsilon_0}{C} \left[\frac{\omega RC}{1 + (\omega RC)^2} \right] \quad (4)$$

where ϵ_0 is the permittivity of free space, 8.854×10^{-14} F cm⁻¹.

As ω_{\max} corresponds to the maximum of the Debye peak for each RC element in parallel, from Equations (3) and (4) we can obtain M''_{\max} and Z''_{\max} ^{8,9}:

$$Z''_{\max} = \frac{R}{2} \quad (5)$$

$$M''_{\max} = \frac{\epsilon_0}{2C} \quad (6)$$

Using the relation $\omega_{\max} = 2\pi f_{\max}$, we can combine Equations (2) and (6) and obtain the resistivity of an RC element through M''_{\max} :

$$R = \frac{M''_{\max}}{\pi f_{\max}} \quad (7)$$

Thus, the magnitude of the resistivity and capacitance of each element can be estimated using both M''_{\max} and Z''_{\max} . However, it is not always possible to observe the Debye peaks of each RC element in the spectra, as their maxima may be outside the frequency range of the measurement, but when such peaks are present, valuable information about the electrical behavior of the material can be obtained.⁸

Apart from spectroscopic representations of Z''/M'' , plots of $\log C'$ versus $\log f$ can also provide direct information about which region is being measured in a given frequency interval. As capacitance is dependent mainly on the thickness of the different regions of the material (Equation 8), the magnitude of C' [$C' \equiv \epsilon' C_0$] can vary by orders of magnitude from one region to another. For example, the bulk of the material usually has values of around 10^{-12} F cm⁻¹, whereas the grain boundary and the sample-electrode interface have capacitance ranges of 10^{-11} – 10^{-9} and 10^{-6} – 10^{-5} F cm⁻¹, respectively¹⁰:

$$C = \frac{\epsilon A}{d} \quad (8)$$

where ϵ is the absolute permittivity [$\epsilon' \cdot \epsilon_0$] being ϵ_0 the permittivity of free space, 8.854×10^{-14} F cm⁻¹, A is the cross-sectional area of the region, and d is the thickness.

The IS technique has been utilized to analyze the regions present in materials, including bulk and grain boundaries, contributing to a better understanding of their electrical behavior. Additionally, it has been employed to study surface processes, such as catalytic reactions, adsorption processes, and mass transfer. This technique provides useful information for the application of these materials as energy sources, coatings, sensors, and in other applications.¹¹⁻¹⁵

Despite being a powerful technique, few papers are found aligning IS with the study of reaction kinetics and mechanisms. For instance, it can be used in investigating methanol oxidation,¹⁶⁻¹⁸ membrane reactors,¹⁹⁻²² and electrocatalytic processes like water splitting²³ and CO oxidation.²⁴⁻²⁶ Typically, in these studies, the electrical properties of materials, such as conductivity, are merely related to specific frequencies,²⁴ without conducting a detailed evaluation of the IS data. Consequently, valuable information about the electrical behavior of the sample during catalytic processes can be missing.²⁵ To ensure a comprehensive understanding of the electrical behavior during these processes, a deeper analysis of IS data is critical.

Our work brings an approach to the use of the IS technique to help explain the mechanism of the CO oxidation reaction, using the $\text{Pr}_2\text{Zr}_{2-x}\text{Fe}_x\text{O}_{7\pm\delta}$ ($x = 0$ and 0.10) system as the reaction catalyst, where the catalytic study was realized in a previous work.²⁷ In this initial study, it was demonstrated that the catalysts synthesized by the solvothermal method were effective for CO oxidation, making it possible to convert 100% of CO into CO_2 at temperatures below 350°C . Moreover, by increasing the Fe concentration in the sample, the catalysis was improved.

The main objective of the present work is to further study the catalytic behavior that takes place inside the reactor, providing valuable information about unknown solid–gas interaction processes that occur on the sample surface by using IS.

2 | EXPERIMENTAL SECTION

The synthesis method, the materials' characterizations, and the catalytic performance are described elsewhere.²⁷ In this work, two different nominal compositions were studied, $\text{Pr}_2\text{Zr}_2\text{O}_7$ and $\text{Pr}_2\text{Zr}_{1.9}\text{Fe}_{0.1}\text{O}_{6.95}$, and they are referred to as PZ and PZF10, respectively. To perform the IS measurements, the powders calcined at 1200°C were uniaxially pressed into 5 mm diameter, 1 mm thick pellets and sintered at 1200°C for 2 h. Opposite faces of the pellets were coated with electrodes made from platinum paste (Pt Ink 6082, Metalor), which was dried and decomposed by gradual heating to 900°C . Samples with the electrode attached were placed in a conductivity jig and measured using an Agilent 4294A analyzer over the frequency range of 40 Hz–13 MHz with an ac voltage of 0.1 V, in atmospheres of dry N_2 , dry O_2 , dry CO, and dry N_2 :CO: O_2 ratio of 23:1:1 (molar basis) gas mixture. The impedance data were corrected for overall pellet geometry.

3 | RESULTS AND DISCUSSION

3.1 | Electrical properties of the fresh samples

To understand the electrical behavior of the compositions prepared, the PZ and PZF10 samples were pressed into pellets, sintered at 1200°C , and covered with Pt paste to perform IS measurements in the range of temperature from room temperature to 400°C . In Figure 1, we can see a typical set of impedance measurements recorded in N_2 dry atmosphere represented in different formats for the two samples analyzed.

The impedance complex plane plots (Figure 1A) recorded in dry N_2 at 300°C show the presence of a single

semicircular arc. The total resistivity obtained from the intercept of the arc with the Z' axis is approximately 1000 k Ω cm for PZ. For the PZF10 sample, it is also possible to notice a single symmetric arc, which intercepts Z' at 450 k Ω cm. The lower overall resistivity of PZF10 can be explained by the increase in defect concentration due to the presence of Fe as a dopant ion. It is noteworthy that the introduction of Fe in substitution of Zr in the PZF10 results in a defect structure that comprises a complex defect consisting of an oxygen vacancy at the corners of two adjacent octahedra: one containing Fe and the other containing Zr. This situation gives a polar complex defect that depending on the iron oxidation state could be represented such as $\text{Fe}'\text{-V}_\text{O}^\bullet$. It is widely acknowledged in the field of surface chemistry that this defect can act as an active center for catalytic activity.²⁸ Therefore, it is of great interest to investigate possible correlations between alterations in the electrical properties of this material and its catalytic property.

Figure 1B,C shows that the Z''/M'' spectroscopic plots exhibit a unique Debye peak in each spectrum with almost coincident maximum peak frequencies for both samples. Therefore, being M'' the inverse of capacitance and more sensitive to the grain response of a ceramic material and Z'' is always dominated by the most resistive component, it is possible to associate that the total resistivity of these samples is dominated by the bulk, and, in a first approximation, these samples can be represented by a simple parallel RC element, indicating that the synthesized materials are electrically homogeneous.

C' data obtained at 300°C for the two compositions are shown in Figure 1D. For PZF10, C' data show two dispersions at high and low frequencies with some evidence of a limiting high-frequency plateau at 5 pF cm^{-1} and a poorly resolved intermediate plateau at approximately 8 pF cm^{-1} (values extracted from the figure). The high-frequency plateau is attributed to the bulk capacitance, whereas the capacitance value for the intermediate plateau is smaller than expected for a grain boundary or surface layer²⁹ but represents an additional element with a small volume fraction resistance that does not contribute to the total resistance $R_T (= R_1)$. This element is speculated to represent the hopping of oxygen vacancies within the dipoles and, therefore, leads to dipole reorientation, but not long-range vacancy migration. It is noteworthy that the dipole reorientation is an ac process that occurs in parallel with the long-range dc conduction.³⁰ On the other hand, the PZ sample at this temperature does not exhibit such a clear pattern, and only a single plateau is visible, but a frequency dispersion is noticeable at low frequencies.

Y' versus $\log f$ plots for both samples at 300°C are shown in Figure 1E. Y' data for the two samples show

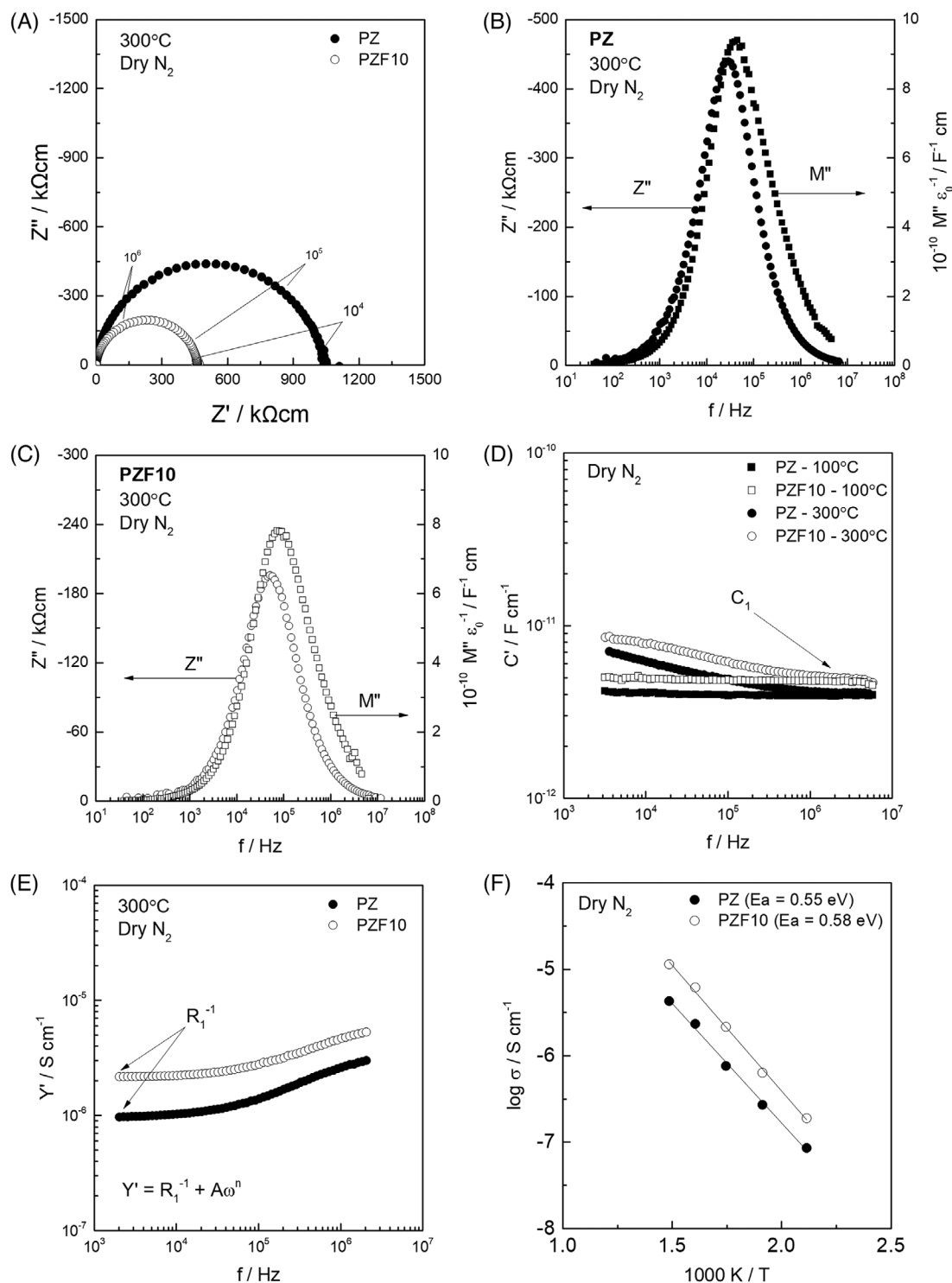


FIGURE 1 (A) Impedance complex plane plots of Z^* at 300°C for PZ and PZF10 samples in dry N_2 . Z''/M'' spectroscopic plots for (B) PZ and (C) PZF10. (D) $C'/\log f$ spectroscopic plot recorded in dry N_2 at 100 and 300°C for PZ and PZF10. (E) $Y'/\log f$ spectroscopic plot recorded in dry N_2 at 300°C for PZ and PZF10. (F) The Arrhenius plot of overall conductivity for both samples in a dry N_2 atmosphere.

a low-frequency plateau corresponding to the dc or bulk conductivity, together with an additional high-frequency power law dispersion, of a particular slope n , when plotted on logarithmic scales, attributed in this case to the Jonscher law behavior.³¹ The onset of a

power law response is seen for frequencies $>10^4$ Hz in Figure 1E for both samples. As part of the same behavior, C' data showed the dispersion toward increasing C' values at lower frequencies, below the high-frequency plateau, where in this case, the slope will be $n-1$ in log

scales.³⁰ This is seen for frequencies over the range 10^4 – 10^6 Hz in Figure 1D. Therefore, both parameters C' and Y' are frequency-dependent in both samples, especially when the temperature is increased over a limited frequency range. Note that the frequency-independent range is usually observed at high frequencies and low temperatures (see Figure 1D).

It is well known that dispersion corresponds to the frequency/time domain region where local conduction processes occur, but on a shorter timescale than lower frequency dc processes. As the frequency in the dispersive range increases, the conduction process is easier to detect, and the measured ac conductivity increases. This dispersion region has been modelled using various empirical functions, but Almond and coworkers^{32,33} demonstrated that the power law dependence is a consequence of an equivalent circuit that consists of a large resistor–capacitor network and, therefore, involves the inclusion of a *constant phase element* (CPE), in the equivalent circuits together with the R and C in parallel, the admittance of which is given by

$$Y * (\text{CPE}) = A\omega^n + jB\omega^n = Y' + jY'' \quad (9)$$

where $0 < n < 1$ and $B/A = \tan n\pi/2$. For a CPE element alone, a spectroscopic plot of Y' versus ω on logarithmic scales is linear, with a slope n and A value equal to Y' when $\omega = 1$. The presence of a CPE in a parallel RC element causes a change in the admittance data, because admittances in parallel are additive,¹⁰ and therefore, for an R -CPE- C circuit, Y^* is given by $Y^* = R^{-1} + A\omega^n + j(B\omega^n + \omega C)$, and Y' has a limiting, frequency-independent conductivity, given by R^{-1} , at low frequencies and on, log scales, a linear increase of slope n , given by CPE, at high frequencies.

The inclusion of this CPE is also necessary due to the shape of the Z'' and M'' peaks. This is clearly observed in the M'' peak of Figure 1B,C, where this peak is Debye-like at frequencies lower than the peak maximum but broadened at higher frequencies.

From the impedance data, the overall sample resistivities were obtained from the intercepts of the arc on the Z' axis in the range 200–400°C and are shown in the Arrhenius plots as a function of the reciprocal temperature in Figure 1F. A linear behavior is observed, with activation energies around 0.55 and 0.58 eV for PZ and PZF10, respectively. Over the entire temperature range, the Fe-doped composition presented a higher conductivity. The conductivity at 400°C in dry N_2 was 4.27×10^{-6} and 1.14×10^{-5} S cm^{-1} for PZ and PZF10, respectively.

A more accurate data analysis of these behaviors will be done later to fit the experimental data to possible equiv-

alent circuits. In this way, we will obtain an equivalent circuit using various formalisms to prove that the adjustment is correct, also obtaining the values of R , C , and CPE for the different components.

3.2 | IS measurements under different atmospheres

In order to understand the electrical behavior of the material in different atmospheres, an experiment was performed where IS measurements were taken at a constant temperature of 300°C first in N_2 , then in O_2 , and finally in CO. Examining the electrical response of the material in inert, oxidizing, and reducing atmospheres enables a more profound comprehension of the conduction mechanisms presented by the prepared samples. All impedance measurements were performed in dry atmospheres, and the total resistivity was recorded after the stabilization of the system at a constant resistivity value.

The effect of different atmospheres on the impedance response is shown in Figure 2A,B for the impedance complex plane plots of both samples at 300°C, and in Supporting Information for the different impedance formalisms, Figure S1. In all cases, only the bulk response is observed, but, as it was appreciated in the measurements under dry N_2 , a dispersion of the C' and Y' data at low and high frequencies, respectively, was observed in all atmospheres (see the Supporting Information section). The overall resistivity values for both compositions were highest in N_2 and lowest in O_2 , as seen clearly in the inset of Figure 2A,B. These figures also show the increase in the total resistivity of both samples when measured in the dry CO atmosphere. Due to the high resistivity in CO, it is not possible to see the closing of the arc in the complex plane plot for the two samples at this temperature.

As the two samples showed variations in the resistivity when the pO_2 is changed, it is possible to assume that there is evidence of an electronic conduction mechanism in both samples for the temperature range studied. Nevertheless, the influence of ionic transport in this material cannot be disregarded, which may also help in the catalytic process. As seen in other pyrochlore structures,^{34–36} these materials can present mixed ionic–electronic conductivity, depending on the conditions of the electrical measurements.

In these samples, the lower resistivity in O_2 can be explained by the absorption of oxygen, decreasing the number of electrons to form O^{2-} ions and, thus, increasing the number of holes (Equation 10). If the holes are the charge carriers involved in the conduction mechanism, the

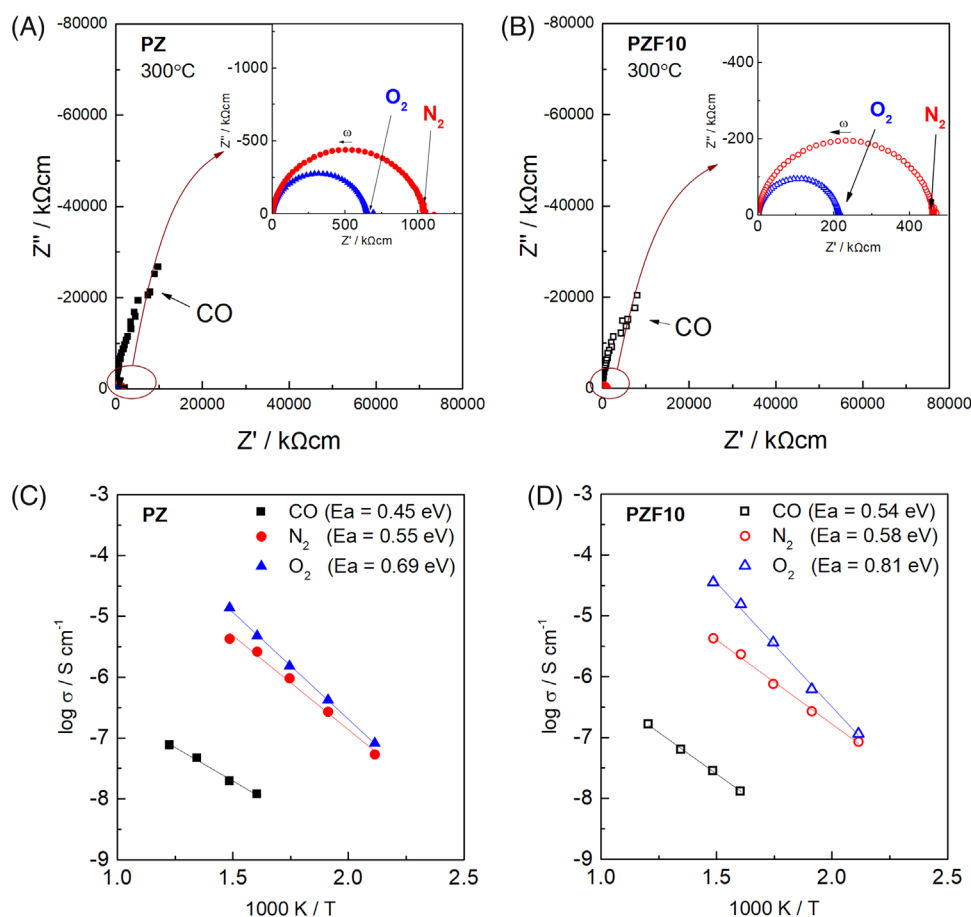
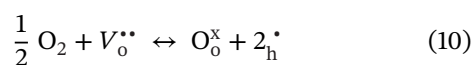


FIGURE 2 Impedance complex plane plots, Z^* , for (A) PZ and (B) PZF10 at 300°C measured in dry N_2 , dry O_2 , and dry CO. Arrhenius plot of overall conductivity for (C) PZ and (D) PZF10 in different dry atmospheres.

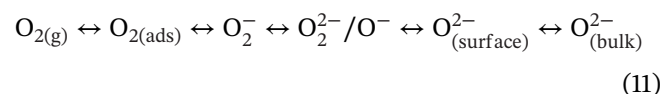
resistance of the sample will decrease, which is a typical behavior of a p-type electronic conductor.³⁷



Once the electrical measurements were carried out at the constant temperature of 300°C in different atmospheres, the experiment was repeated but obtaining the data as a function of temperature in the range of 100–450°C for the three atmospheres studied. As in the previous measures, the data were recorded first in N_2 , then in O_2 , and finally in CO. From the impedance complex plane plots, Z^* , the total resistivity was obtained in each case, and the data were represented in the Arrhenius format, as can be seen in Figure 2C,D. As before, the conductivity was higher in dry O_2 , decreasing in dry N_2 and in dry CO for both samples.

Analyzing the data obtained from the Arrhenius plots for both samples, it is possible to notice a linear behavior in all cases but with different activation energies (E_a) depending on the atmosphere, being higher in O_2 and lower in N_2 and CO. Thus, the lower activation energy observed in dry N_2 and CO together with the obtention of nonparallel

Arrhenius plots, suggests that the conduction mechanism in each atmosphere is slightly different. Assuming that the conductivity, σ , can be described by the product of carrier concentration, n , electronic charge, e , and the mobility, μ , ($\sigma = ne\mu$), in this case, as described in Equation (10), the increase of conductivity under O_2 , leads to an increase of the carrier concentration. Moreover, it is well known that under specific conditions, like under O_2 , anionic species such as superoxide or peroxide could be present in the surface of the material, promoting the electronic conduction in the system and also increasing the conductivity of the sample.^{38–40} Equilibria between various species can be represented by the following equation:



Reactions where oxygen species (O_2^- , O_2^{2-}/O^- , O^{2-}) are formed involve electron transfer between oxygen species that originate from the gas phase and electrons from the sample. Thus, electrons are withdrawn from the

near-surface sample lattice and are trapped at the sample surface as increasingly reduced oxygen species. Usually, the presence of these oxygen species has no direct influence on the overall bulk properties. However, if there are displacements in the equilibria described in Equation (11), resulting in changes in electron concentration, particularly in insulating or poorly conductive materials (as is the case with this material), it can lead to spontaneous changes in sample conductivity.^{38–40} In CO atmosphere, Pr^{4+} and Fe^{3+} ions are reduced to Pr^{3+} and Fe^{2+} ,⁴¹ decreasing the number of charge carriers responsible for the conduction of these materials, and also the equilibrium of Equation (11) may be displaced in the reversible direction.

The enhanced conductivity of PZF10 in comparison to PZ can be attributed to the introduction of the dopant, Fe, into the structure. The presence of Fe generates additional holes in the valence band, leading to an increased number of available charge carriers and consequently, a higher electronic conductivity in the material. Furthermore, the dopant ions can induce defects in the crystal lattice, such as oxygen vacancies, which further contribute to the improved electrical conductivity. These defects create localized electronic states within the band gap, serving as trap sites for charge carriers and facilitating their movement through the material. As a result, the combination of additional charge carriers and defect-induced conductivity enhances the overall electrical properties of PZF10 compared to PZ. A more detailed study on the effect of Fe as a dopant in the electrical properties of this system is available elsewhere.⁴¹

3.3 | IS measurements in an $\text{N}_2:\text{CO}:\text{O}_2$ gas mixture

In previously published studies carried out with these materials,²⁷ a good catalytic activity was observed for the CO oxidation reactions. The catalytic findings for this process revealed that higher Fe concentration led to an enhancement in catalytic activity. Additionally, the reaction occurred within a narrow temperature range as the concentration of Fe increased. Notably, a complete conversion of $\text{CO}-\text{CO}_2$ was achieved at 341°C for PZ composition and at 257°C for PZF10 composition.

In order to simulate the CO oxidation reaction and follow it by IS measurements, a mixture of $\text{N}_2:\text{CO}:\text{O}_2$ with a molar ratio of 23:1:1 was prepared. Impedance measurements were then carried out while increasing the temperature from 200 to 400°C . After the measurements were completed, the impedance data were analyzed to obtain the equivalent circuit for each case. Figure 3 shows a selection of the impedance data at various temperatures, along with the corresponding fitting.

In the temperature range and atmospheres studied, the impedance data are always dominated by the bulk response of the sample. The complex plane plot (a and b) shows a single undistorted semicircle with almost Debye-like overlapping peaks in the Z''/M'' spectra (c and d), indicating that the sample is electrically homogeneous and contains essentially one electrical component. As previously observed, a dispersion of the C' and Y' data at low and high frequencies, respectively, was noticed in these measurements. For the PZF10 sample, a poorly resolved plateau was observed at the highest temperatures, with a capacitance value of approximately 8 pF cm^{-1} at 300°C . In a first approximation, this could be associated with a dipole relaxation process.^{30,42}

After extracting the impedance data, the analysis was performed by fitting the data to find the most appropriate equivalent circuit to represent the data sets. All formalisms of impedance were used, including $\log Y'$ versus $\log f$ plots and $\log C'$ versus $\log f$, to decide the best equivalent circuit.

The $\log Y'$ versus $\log f$ plots provided information about the conductive element and highlighted the presence of a high-frequency power law dispersion, which was modeled using the bulk CPE.

On the other hand, information about the capacitive elements was extracted from the $\log C'$ versus $\log f$ plots, which allowed the observation of the poorly resolved plateau at the highest temperatures associated with a dielectric element in the PZF10 sample. This was considered in the equivalent circuit of this sample, including a C and R in series (C_2-R_2).

Therefore, to obtain a good quality fit of the experimental data in all the spectroscopic plots using the equivalent circuits, it was necessary to use only a combination of R_1 -CPE $_1$ - C_1 for the PZ sample, whereas, for the PZF10 sample, the inclusion of the R_2 - C_2 element was necessary to have a good fitting due to the appearance of a poorly resolved plateau.

From the fittings made, different values of R and C were obtained in each case, as well as the A and n parameters of the CPE. Table S1 summarizes the data obtained for the two samples at different temperatures.

To relate the data obtained from the IS and the CO conversion results published previously, the resistance values, R_1 , obtained from the fitting were represented against temperature together with the CO conversion results in %²⁷ for the two samples studied (Figure 4A,B).

The data obtained for the PZ sample, represented in Figure 4A, show a pronounced change in the total resistivity of about an order of magnitude in the temperature range from 280 to 300°C , which coincides with the beginning of the catalytic process. As the temperature increases, the resistivity continues to slightly decrease, and

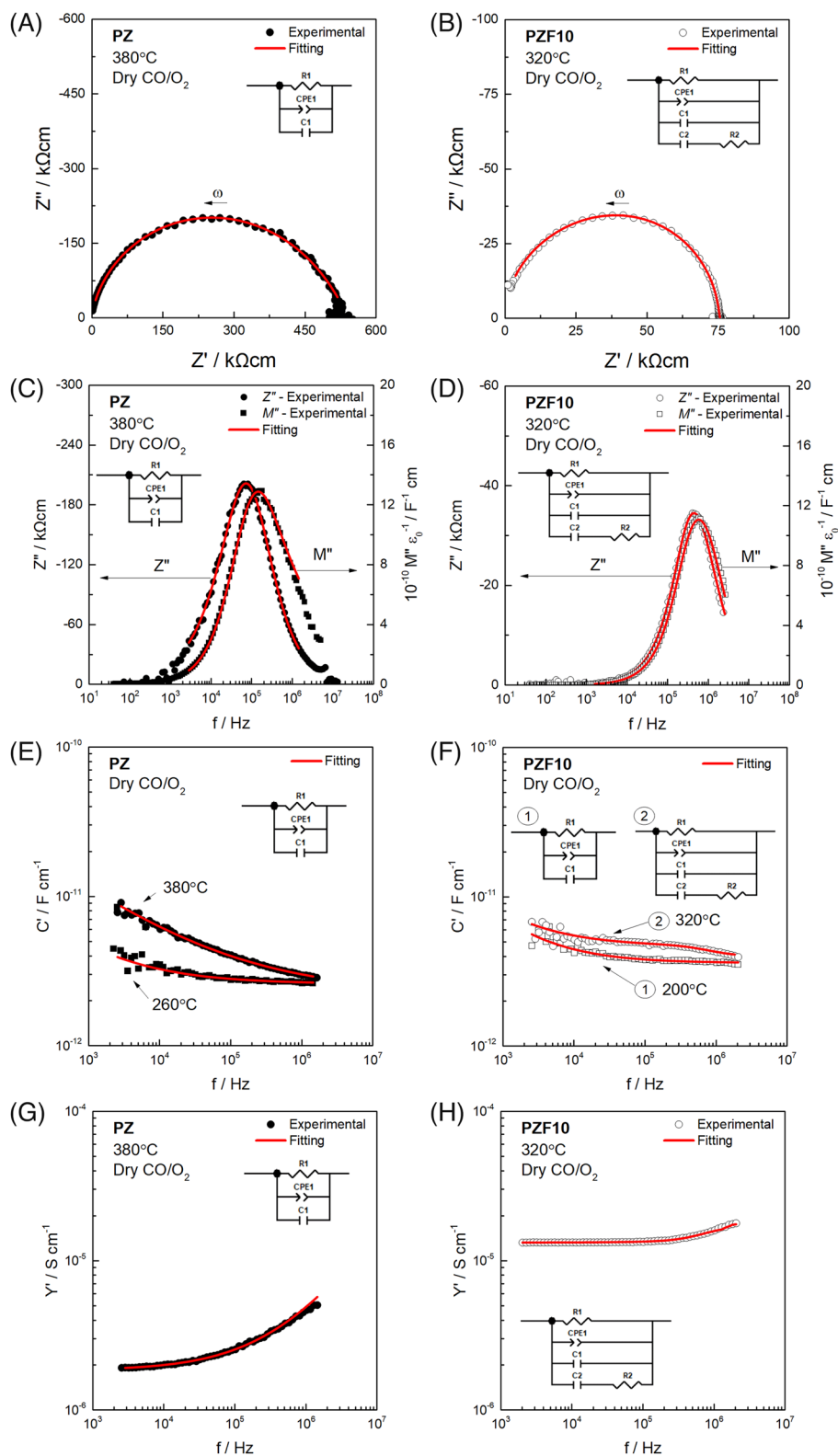


FIGURE 3 Experimental data and fits to the equivalent circuits (inset of figures) for impedance complex plane plots, Z^* (a and b), and spectroscopic plots of (c and d) Z''/M'' , (e and f) C' and, (f and g) Y' at different temperatures; $\omega = 2\pi f$.

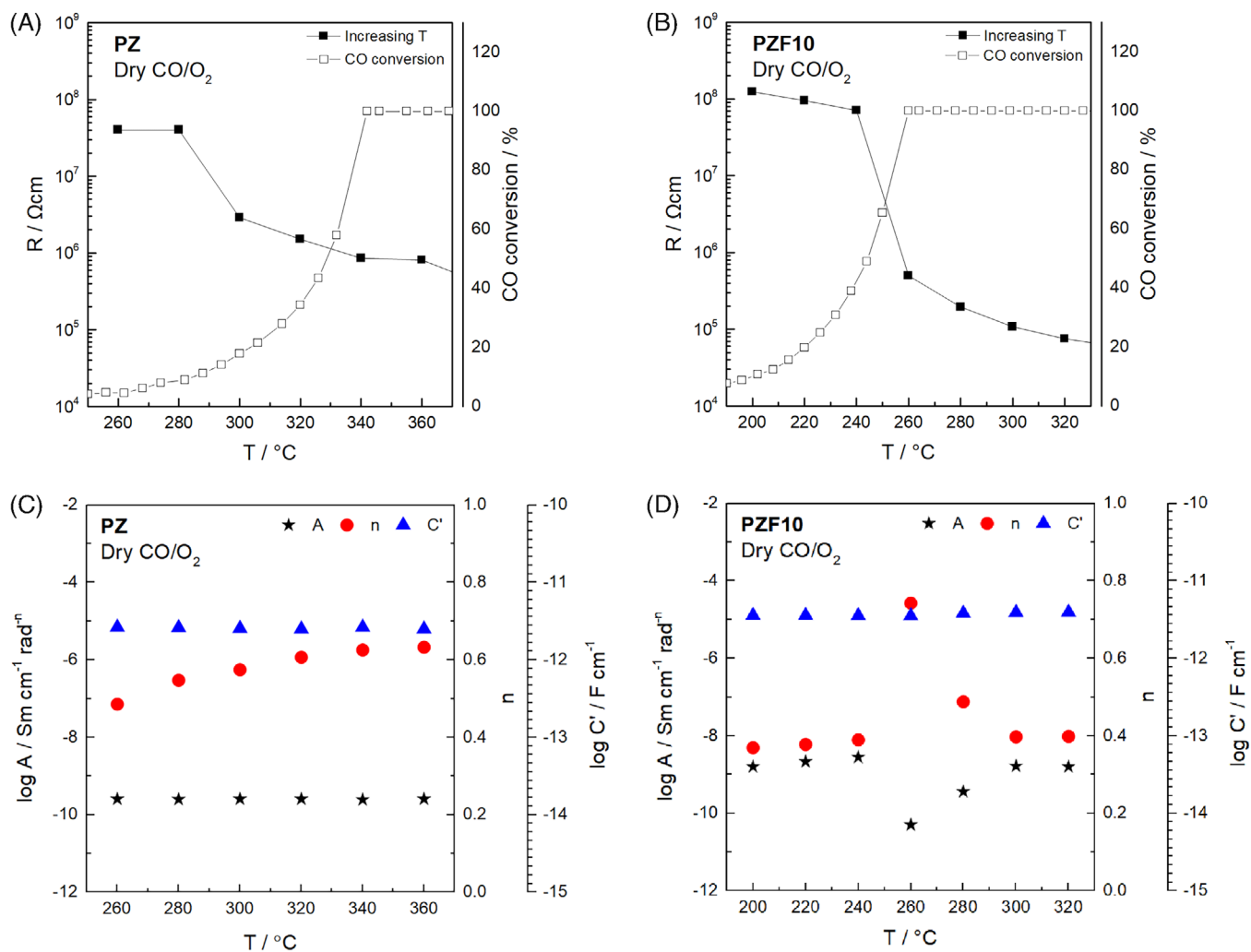


FIGURE 4 (a and b) Evolution of the bulk resistivity, R_1 , under dry N_2 :CO:O₂ (23:1:1) atmosphere and CO conversion in % as a function of temperature. (c and d) Fitted parameters A_1 and n of CPE₁, and C_1 for PZ and PZF10 samples.

the CO oxidation reaction is completed at an approximate temperature of 340°C.

For the PZF10 sample (Figure 4B), there is a drastic decrease in the resistivity in the temperature range of 240–260°C. Analyzing the results of CO conversion together with the IS measurements, it is interesting to point out that the most pronounced moment of the oxidation reaction occurs in the same temperature range in which there is a decrease in the resistivity of the material. These results suggest a possible connection between the change in resistivity and the CO conversion. In a previous work,²⁵ employing CeO₂ as a catalyst, a similar correlation between the temperature of CO oxidation and a decrease in resistivity was observed at a fixed temperature (450°C) over time. In the present study on pyrochlores, the dependence of the CO oxidation and the electrical properties was investigated as the temperature increased, providing more in-depth IS data. Such information can contribute to the interpretation of the catalytic reaction process using

these materials, particularly when evaluating the impact of incorporating a dopant into the crystalline structure.

For the composition PZ, a mixture of Pr³⁺ and Pr⁴⁺ species is expected after the calcination process.⁴¹ During the catalytic reaction, where both O₂ and CO are present, first, there is an adsorption of oxygen on the grain surface of the catalyst, which is justified by the decrease in resistivity, as this system behaves as a p-type semiconductor in the selected temperature range. The CO molecules react with the oxygen species located in low-coordinated sites on the catalyst grain surface to form CO₂. At the same time, similar to the case of CeO₂,^{43–45} CO₂ could oxidize Pr³⁺ to Pr⁴⁺, which increases the number of charge carriers (holes) and decreases the overall resistivity, as shown in Figure 4A. Furthermore, under a more oxidizing atmosphere, such as CO₂/O₂, the presence of oxygen reactive species on the surface of the material, such as superoxide or peroxide (Equation 11), can also promote a decrease in resistivity.

In addition to a mixture of Pr^{3+} and Pr^{4+} ions, in the PZF10 sample, there is also a mixture of Fe^{3+} and Fe^{2+} species. As seen in the IS measurements (Section 3.1), the lower resistivity of this sample in comparison to the PZ is due to the substitution of Zr^{4+} by Fe^{3+} , generating structural defects. These structural defects cause a charge deficiency in the material, facilitating the entry of oxygen on the subsurface lattice. This behavior was confirmed in the previous work²⁷ by XPS, where the results showed that the PZF10 fresh sample (before reaction) had a higher concentration of oxygen species in the lattice in comparison with the oxygen species present in the surface.

The sudden change in resistivity of the PZF10 sample in the temperature range from 240 to 260°C shown in Figure 4B is possibly due to different factors. First, a lower initial oxygen concentration is adsorbed; thus, more active sites at the beginning of the reaction. On the other hand, there are also more species susceptible to suffer oxidation/reduction, due to the higher concentration of Pr^{4+} and also the presence of Fe^{3+} . Another factor that is present in this whole process is the charge deficiency of the material, which facilitates the exchange of oxygen in the solid–gas interface, as the energy cost to create a vacant center near a low-valence dopant is lower than that on the undoped surface.⁴⁶ At the same time, the PZF10 sample may present more reactive oxygen species, when the CO is oxidized to CO_2 , increasing the $p\text{O}_2$. All these factors lead the PZF10 sample to show catalytic activity in a lower temperature range than the PZ sample.

An important result, which to our knowledge has never been reported, and that can help identify the temperature range in which redox processes occur in the material, leading to the catalysis of the reaction, is the observation of the parameters of power law dispersion from the impedance spectroscopic plots. This dispersion, as indicated above, is extracted by obtaining the data from a fit that includes a CPE_1 in the equivalent circuit and corresponds to regions where the local conduction process occurs; therefore, this could be more affected when the number of defects is greater. Figure 4C,D shows the values of A and n , as well as the bulk capacity, obtained from the adjustment of the impedance data (Table S1), as a function of temperature. As observed for the PZF10 sample, the highest value of n and the lowest value for A were obtained at the temperature where the catalytic process reached the higher percent of conversion, increasing or decreasing until this point. At this point, the resistivity for this sample also decreased by two orders of magnitude. This effect is less pronounced in the PZ sample, where the number of defects is lower, and the resistivity change is also less. It is important to note that the capacitance of the bulk remains constant across all temperature ranges studied.

So, the better catalytic activity of the PZF10 sample is a set of factors, going from the electronic deficiency caused by the incorporation of Fe in the structure, which leads to a higher number of oxygen vacancies and a better oxygen exchange at the solid–gas interface, as well as the redox behavior of Pr/Fe and oxygen species. The $\text{Fe}'\text{-V}_\text{o}$ defect complex present in the PZF10 sample acts as an active site for the adsorption of gas-phase species, including O_2 and CO. This process leads to the formation of intermediates, as described in Equation (11). The formation of these species involves electron transfer, originating from both Pr and Fe in the lattice, as well as from the adsorption of CO molecules. As a result, increasing the concentration of these active species enhances the catalytic activity of the PZF10 sample. As demonstrated in previous studies involving different types of materials found in the literature, these factors play a crucial role in the oxidation of CO.^{47–51}

Figure 5 represents the overall process, from the influence of Fe substitution on the Zr site in the pyrochlore structure and the electrical response of the sample at different $p\text{O}_2$ (Figure 5A) to the behavior of the material as a catalyst for the CO oxidation reaction (Figure 5B).

Therefore, this work demonstrates that combining IS with catalytic reactions provides a robust approach to comprehensively understand the mechanism involved in catalysis and enables a precise analysis of changes that occur in the solid–gas interface. The identification of different parameters obtained from impedance data analysis not only helps to understand the catalytic processes of the studied materials but also any similar materials. This approach offers an improvement in the understanding of catalytic reactions and opens up new possibilities for their optimization and design.

4 | CONCLUSION

This study investigated the catalytic behavior of $\text{Pr}_2\text{Zr}_2\text{O}_7$ and $\text{Pr}_2\text{Zr}_{1.9}\text{Fe}_{0.1}\text{O}_{6.95}$ (referred to as PZ and PZF10) nominal compositions using IS. The measurements in different atmospheres showed that both samples exhibited a p-type conduction mechanism, with higher conductivity in dry O_2 and decreasing conductivity in dry N_2 and dry CO.

To simulate the CO oxidation reaction, IS measurements were carried out in a dry $\text{N}_2:\text{CO}:\text{O}_2$ (23:1:1 molar basis) mixture, and the data were fitted using the most appropriate equivalent circuit to represent the data sets. The resistance values obtained from the fitting for the PZ sample showed a gradual decrease in total resistivity as the temperature increased in the range from 280 to 360°C. For the PZF10 sample, there was a more pronounced decrease in resistivity in the temperature range of 240–260°C. Upon analyzing

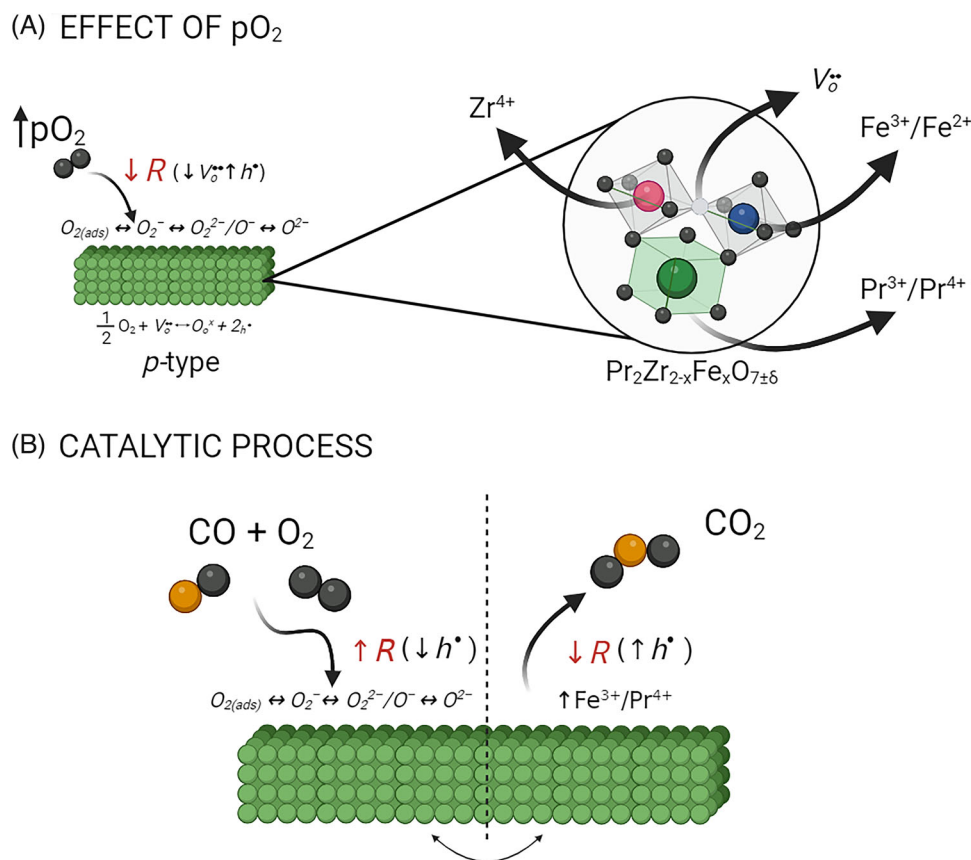


FIGURE 5 (A) Structural representation of the Fe substitution on the Zr site in the pyrochlore structure and the effect of different pO_2 on the electrical response of the system. (B) Scheme of the material behavior as a heterogeneous catalyst for the CO oxidation reaction and the change of the electrical response. Source: Created with BioRender.com.

the CO conversion results along with the IS measurements, it is noteworthy that the catalysis of the reaction occurred in the same temperature range where there was a decrease in material resistivity.

Moreover, an important previously unreported finding is that it is possible to identify the temperature range where the catalysis occurs by examining the parameters of power law dispersion derived from impedance spectroscopic plots. This range, where a change in the A and n parameters is observed, coincides with the maximum moment of the catalytic process for CO oxidation, particularly in the case of the PZF10 sample. The calculated values of the power law dispersion, which are represented by CPE_1 in the equivalent circuit, could be directly related to the increase in the number of defects in the structure. These values were obtained for both samples and showed dependence on temperature. The values of A and n showed the highest variation in the temperature range of the CO oxidation reaction for sample PZF10, which has a higher number of defects.

Based on the data collected by the IS measurements, the catalytic reaction mechanism can be explained as follows: For the PZ composition, during the reaction,

oxygen molecules are adsorbed on the grain surface of the catalyst, which is evident from the decrease in resistivity, as this system acts as a p-type semiconductor. Subsequently, CO molecules react with the reactive oxygen species, such as superoxide or peroxide, which are located at the low-coordinated sites on the catalyst's surface, to form CO_2 . At the same time, the newly generated CO_2 can oxidize Pr^{3+} to Pr^{4+} , which increases the number of charge carriers (holes) and contributes to the reduction in overall resistivity. In the case of the PZF10 sample, the sudden change in resistivity in the temperature range from 240 to 260°C is possibly due to more active sites at the beginning of the reaction, more species susceptible to suffer oxidation/reduction and higher number of oxygen vacancies in comparison with the PZ sample.

These results demonstrate that combining IS with catalytic reactions provides a robust approach to comprehensively understand the mechanism involved in catalysis and enables a precise analysis of changes that occur in the solid-gas interface. The identification of different parameters obtained from impedance data analysis not only helps to understand the catalytic processes of the


studied materials but is also an interesting tool for the study of other heterogeneous catalysts.

ACKNOWLEDGMENTS

H.B.-M., E.C., and E.L.S.V. thank the Spanish Ministerio de Ciencia e Innovación [Project PID2020-116149GB-I00] for the financial support. E.L.S.V. thanks the Generalitat Valenciana [GRISOLIA/2019/054] for the predoctoral contract. X.V. is a Serra Húnter Fellow and is grateful to the Generalitat de Catalunya. J.L. is a Serra Húnter Fellow and is grateful to the ICREA Academia program and projects MICINN/FEDER PID2021-124572OB-C31 and GC 2021 SGR 01061.

ORCID

Emerson Luiz dos Santos Veiga  <https://orcid.org/0000-0001-6210-2481>

Héctor Beltrán-Mir  <https://orcid.org/0000-0002-7836-1602>

Xavier Vendrell  <https://orcid.org/0000-0003-4705-8253>

REFERENCES

- Macdonald JR, Johnson WB. Fundamentals of impedance spectroscopy. In: Impedance spectroscopy. Hoboken: Wiley; 2005. p. 1–26. <https://doi.org/10.1002/0471716243.ch1>
- Lvovich VF. Impedance spectroscopy: applications to electrochemical and dielectric phenomena. John Wiley & Sons, Hoboken, New Jersey, United States of America, 2012.
- Irvine JTS, Sinclair DC, West AR. Electroceramics: characterization by impedance spectroscopy. *Adv Mater.* 1990;2(3):132–38. <https://doi.org/10.1002/adma.1990020304>
- Aljarrah M, Salman F. A simple analysis of impedance spectroscopy: review. *J Inst Eng (India): A: Ser D.* 2021;102(1):237–42. <https://doi.org/10.1007/s40033-021-00252-7>
- Kanoun O. Impedance spectroscopy advances and future trends: a comprehensive review. In: Impedance spectroscopy: advanced applications: battery research, bioimpedance, system design. Berlin, Germany: De Gruyter; 2018. p. 1–21. <https://doi.org/10.1515/9783110558920-001>
- Heath JP, Harding JH, Sinclair DC, Dean JS. The analysis of impedance spectra for core-shell microstructures: why a, multiformalism approach is essential. *Adv Funct Mater.* 2019;29(38):1904036. <https://doi.org/10.1002/adfm.201904036>
- West AR. Solid state chemistry and its applications. 2nd ed. West Sussex, UK: John Wiley & Sons, Ltd; 2014.
- Morrison FD, Sinclair DC, West AR. Characterization of lanthanum-doped barium titanate ceramics using impedance spectroscopy. *J Am Ceram Soc.* 2001;84(3):531–38. <https://doi.org/10.1111/j.1151-2916.2001.tb00694.x>
- Sinclair DC. Characterization of electro-materials using ac impedance spectroscopy. *Boletín de la Sociedad Española de Cerámica y Vidrio.* 1995;34(2):55–65.
- West AR. Solid state chemistry and its applications. 2nd ed. Hoboken, NJ: John Wiley & Sons; 2022.
- Lasia A. Electrochemical impedance spectroscopy and its applications. New York, NY: Springer New York; 2014. https://doi.org/10.1007/978-1-4614-8933-7_1
- Yang F, Xiao P. Nondestructive evaluation of thermal barrier coatings using impedance spectroscopy. *Int J Appl Ceram Technol.* 2009;6(3):381–99. <https://doi.org/10.1111/j.1744-7402.2008.02304.x>
- de León SE, Pupovac A, McArthur SL. Three-dimensional (3D) cell culture monitoring: opportunities and challenges for impedance spectroscopy. *Biotechnol Bioeng.* 2020;117(4):1230–40. <https://doi.org/10.1002/bit.27270>
- Tenreiro AFG, Lopes AM, da Silva LFM. A review of structural health monitoring of bonded structures using electromechanical impedance spectroscopy. *Struct Health Monit.* 2022;21(2):228–49. <https://doi.org/10.1177/1475921721993419>
- Gu W, Zhao Y. Cellular electrical impedance spectroscopy: an emerging technology of microscale biosensors. *Expert Rev Med Devices.* 2010;7(6):767–79. <https://doi.org/10.1586/erd.10.47>
- Holm T, Sunde S, Seland F, Harrington DA. Understanding reaction mechanisms using dynamic electrochemical impedance spectroscopy: methanol oxidation on Pt. *Electrochim Acta.* 2019;323:134764. <https://doi.org/10.1016/j.electacta.2019.134764>
- Holm T, Dahlstrom PK, Sunde S, Seland F, Harrington DA. Dynamic electrochemical impedance study of methanol oxidation at Pt at elevated temperatures. *Electrochim Acta.* 2019;295:139–47. <https://doi.org/10.1016/j.electacta.2018.10.071>
- Ugalde-Reyes O, Liu HB, Roquero P, Alvarez-Ramirez J, Sosa-Hernández E. EIS and relaxation times study for CO adsorbed on bimetallic Pt-Mo catalysts during the methanol oxidation reaction. *Electrochim Acta.* 2022;418:140309. <https://doi.org/10.1016/j.electacta.2022.140309>
- Zhang H, Suresh A, Carter CB, Wilhite BA. Electrochemical, catalytic and O₂-permeation studies of iron-doped barium zirconates for membrane reactor applications. *ECS Trans.* 2014;61(1):307–18. <https://doi.org/10.1149/06101.0307ecst>
- Wagner N. Characterization of membrane electrode assemblies in polymer electrolyte fuel cells using a.c. impedance spectroscopy. *J Appl Electrochem.* 2002;32(8):859–63. <https://doi.org/10.1023/A:1020551609230>
- Pivac I, Bezmalinović D, Barbir F. Catalyst degradation diagnostics of proton exchange membrane fuel cells using electrochemical impedance spectroscopy. *Int J Hydrogen Energy.* 2018;43(29):13512–20. <https://doi.org/10.1016/j.ijhydene.2018.05.095>
- Meyer Q, Zeng Y, Zhao C. Electrochemical impedance spectroscopy of catalyst and carbon degradations in proton exchange membrane fuel cells. *J Power Sources.* 2019;437:226922. <https://doi.org/10.1016/j.jpowsour.2019.226922>
- Anantharaj S, Noda S. Appropriate use of electrochemical impedance spectroscopy in water splitting electrocatalysis. *ChemElectroChem.* 2020;7(10):2297–308. <https://doi.org/10.1002/celec.202000515>
- Vasile A, Bratan V, Hornoiu C, Caldararu M, Ionescu NI, Yuzhakova T, et al., Electrical and catalytic properties of cerium-tin mixed oxides in CO depollution reaction. *Appl Catal B.* 2013;140–1:25–31. <https://doi.org/10.1016/j.apcatb.2013.03.042>
- Vendrell X, Kubyshev Y, Mestres L, Llorca J. Co oxidation on ceria studied by electrochemical impedance

- spectroscopy. *ChemCatChem*. 2020;12(23):5926–31. <https://doi.org/10.1002/cctc.202001389>
26. Sugimoto W, Aoyama K, Kawaguchi T, Murakami Y, Takasu Y. Kinetics of CH₃OH oxidation on PtRu/C studied by impedance and CO stripping voltammetry. *J Electroanal Chem*. 2005;576(2):215–21. <https://doi.org/10.1016/j.jelechem.2004.10.018>
 27. dos Santos Veiga EL, Villafruela XV, Llorca J, Beltrán-Mir H, Cordoncillo E. The catalytic activity of the Pr₂Zr_{2-x}Fe_xO_{7±δ} system for the CO oxidation reaction. *J Am Ceram Soc*. 2022;106:1369–80. <https://doi.org/10.1111/jace.18846>
 28. Trovarelli A, Llorca J. Ceria catalysts at nanoscale: how do crystal shapes shape catalysis? *ACS Catal*. 2017;7(7):4716–35. <https://doi.org/10.1021/acscatal.7b01246>
 29. Jovaní M, Beltrán-Mir H, Cordoncillo E, West AR. Field-induced p-n transition in yttria-stabilized zirconia. *Sci Rep*. 2019;9(1):18538. <https://doi.org/10.1038/s41598-019-54588-y>
 30. Ramírez-González J, West AR. Electrical properties of calcia-stabilised zirconia ceramics. *J Eur Ceram Soc*. 2020;40(15):5602–11. <https://doi.org/10.1016/j.jeurceramsoc.2020.06.023>
 31. Jonscher AK. Dielectric relaxation in solids. *J Phys D Appl Phys*. 1999, 32(14):R57–R70. <https://doi.org/10.1088/0022-3727/32/14/201>
 32. Almond D, West A. Mobile ion concentrations in solid electrolytes from an analysis of a.c. conductivity. *Solid State Ion*. 1983;9–10:277–82. [https://doi.org/10.1016/0167-2738\(83\)90247-3](https://doi.org/10.1016/0167-2738(83)90247-3)
 33. Almond DP, Hunter CC, West AR. The extraction of ionic conductivities and hopping rates from a.c. conductivity data. *J Mater Sci*. 1984;19(10):3236–48. <https://doi.org/10.1007/BF00549810>
 34. van Dijk MP, de Vries KJ, Burggraaf AJ. Oxygen ion and mixed conductivity in compounds with the fluorite and pyrochlore structure. *Solid State Ion*. 1983;9–10:913–19. [https://doi.org/10.1016/0167-2738\(83\)90110-8](https://doi.org/10.1016/0167-2738(83)90110-8)
 35. Shimura T, Komori M, Iwahara H. Ionic conduction in pyrochlore-type oxides containing rare earth elements at high temperature. *Solid State Ion*. 1996;86–8:685–89. [https://doi.org/10.1016/0167-2738\(96\)00148-8](https://doi.org/10.1016/0167-2738(96)00148-8)
 36. Tuller H. Mixed ionic-electronic conduction in a number of fluorite and pyrochlore compounds. *Solid State Ion*. 1992;52(1–3):135–46. [https://doi.org/10.1016/0167-2738\(92\)90099-B](https://doi.org/10.1016/0167-2738(92)90099-B)
 37. Gil Escrig L, Prades M, Beltrán H, Cordoncillo E, Masó N, West AR. Voltage-dependent bulk resistivity of SrTiO₃: mg ceramics. *J Am Ceram Soc*. 2014;97(9):2815–24. <https://doi.org/10.1111/jace.13004>
 38. Ren P, Masó N, West AR. Hole conductivity in oxygen-excess BaTi_{1-x}Ca_xO_{3-x+δ}. *Phys Chem Chem Phys*. 2013;15(48):20943. <https://doi.org/10.1039/c3cp52475b>
 39. Vendrell X, West AR. Induced p-type semiconductivity in yttria-stabilized zirconia. *J Am Ceram Soc*. 2019;102(10):6100–6106. <https://doi.org/10.1111/jace.16492>
 40. Gellings PJ, Bouwmeester HJM. Ion and mixed conducting oxides as catalysts. *Catal Today*. 1992;12(1):1–101. [https://doi.org/10.1016/0920-5861\(92\)80046-P](https://doi.org/10.1016/0920-5861(92)80046-P)
 41. dos S Veiga EL, Fortuño-Morte M, Beltrán-Mir H, Cordoncillo E. Effect of the oxidation states on the electrical properties of Fe-doped Pr₂Zr₂O₇ pyrochlore. *J Mater Res Technol*. 2022;16:201–15. <https://doi.org/10.1016/j.jmrt.2021.11.146>
 42. Vendrell X, West AR. Electrical Properties of yttria-stabilized zirconia, YSZ single crystal: local AC and long range DC conduction. *J Electrochem Soc*. 2018;165(11):F966–75. <https://doi.org/10.1149/2.088181jes>
 43. Demoulin O, Navez M, Mugabo J-L, Ruiz P. The oxidizing role of CO₂ at mild temperature on ceria-based catalysts. *Appl Catal B*. 2007;70(1–4):284–93. <https://doi.org/10.1016/j.apcatb.2005.12.024>
 44. Yamaguchi D, Tang L, Scarlett N, Chiang K. The activation and conversion of carbon dioxide on the surface of zirconia-promoted ceria oxides. *Chem Eng Sci*. 2020;217:115520. <https://doi.org/10.1016/j.ces.2020.115520>
 45. Fine GF, Cavanagh LM, Afonja A, Binions R. Metal oxide semiconductor gas sensors in environmental monitoring. *Sensors*. 2010;10(6):5469–502. <https://doi.org/10.3390/s100605469>
 46. Puigdollers AR, Schlexer P, Tosoni S, Pacchioni G. Increasing oxide reducibility: the role of metal/oxide interfaces in the formation of oxygen vacancies. *ACS Catal*. 2017;7(10):6493–513. <https://doi.org/10.1021/acscatal.7b01913>
 47. Chen W, Xu J, Huang F, Zhao C, Guan Y, Fang Y, et al., CO oxidation over CuOx/TiO₂ catalyst: the importance of oxygen vacancies and Cu⁺ species. *Appl Surf Sci*. 2023;618:156539. <https://doi.org/10.1016/j.apsusc.2023.156539>
 48. Lin J, Huang Y, Li L, Wang A, Zhang W, Wang X, et al., Activation of an Ir-in-CeO₂ catalyst by pulses of CO: the role of oxygen vacancy and carbonates in CO oxidation. *Catal Today*. 2012;180(1):155–60. <https://doi.org/10.1016/j.cattod.2011.03.066>
 49. Wang B-J, Chu G-W, Li Y-B, Duan X-Z, Wang J-X, Luo Y. Intensified micro-mixing effects on evolution of oxygen vacancies of CeO₂-based catalysts for improved CO oxidation. *Chem Eng Sci*. 2021;244:116814. <https://doi.org/10.1016/j.ces.2021.116814>
 50. Chen C-S, Chen T-C, Wu H-C, Wu J-H, Lee J-F. The influence of ceria on Cu/TiO₂ catalysts to produce abundant oxygen vacancies and induce highly efficient CO oxidation. *Catal Sci Technol*. 2020;10(13):4271–81. <https://doi.org/10.1039/D0CY00792G>
 51. Zhang J, Wang D, Lai L, Fang X, Xu J, Xu X, et al., Probing the reactivity and structure relationship of Ln₂Sn₂O₇ (Ln = La, Pr, Sm and Y) pyrochlore catalysts for CO oxidation. *Catal Today*. 2019;327:168–76. <https://doi.org/10.1016/j.cattod.2018.05.009>

SUPPORTING INFORMATION

Additional supporting information can be found online in the Supporting Information section at the end of this article.

How to cite this article: dos Santos Veiga EL, Beltrán-Mir H, Vendrell X, Llorca J, Cordoncillo E. Impedance spectroscopy: A useful technique to unveil the mechanism of a CO oxidation reaction. *J Am Ceram Soc*. 2024;107:321–333. <https://doi.org/10.1111/jace.19455>